PHOTONICS Research

Compact low-birefringence polarization beam splitter using vertical-dual-slot waveguides in silicon carbide integrated platforms

Xiaodong Shi,[1] Jingjing Zhang,[2] Weichen Fan,[1] Yaoqin Lu,[1] Nianhua Peng,[3] Karsten Rottwitt,[1] and Haiyan Ou[1,*]

[1]DTU Fotonik, Technical University of Denmark, DK-2800 Lyngby, Denmark
[2]Institute of Mirco/Nano Optoelectronic and Terahertz Technology, Jiangsu University, Zhenjiang 212013, China
[3]Surrey Ion Beam Centre, Surrey University, Guildford, GU2 7XH, UK
*Corresponding author: haou@fotonik.dtu.dk

Received 20 September 2021; revised 15 November 2021; accepted 17 November 2021; posted 18 November 2021 (Doc. ID 443543); published 22 December 2021

The polarization beam splitter is a key component for polarization manipulation in photonic integrated circuits, but it is challenging to design for low-refractive-index optical materials, due to the low birefringence of the waveguides. We propose what we believe is a novel compact vertical-dual-slot waveguide-based coupling scheme for silicon carbide, enabling efficient low-birefringence polarization splitting by extensively modulating the transverse-magnetic mode distribution. We numerically and experimentally demonstrate the device in the 4H-silicon-carbide-on-insulator integrated platform, with a small footprint of 2.2 μm × 15 μm. The device, easy to fabricate via a single lithography process as other components on the chip, exhibits low insertion loss of <0.71 dB and <0.51 dB for the transverse-electric and transverse-magnetic polarized light, respectively, and polarization extinction ratio of >13 dB, over 80 nm wavelength range.

https://doi.org/10.1364/PRJ.443543

1. INTRODUCTION

Silicon carbide (SiC) has attracted great interest in both classical and quantum integrated photonics during the past decade, thanks to its wide bandgap, excellent second- and third-order nonlinear properties, and a variety of intrinsic color centers [1,2]. These characteristics have been employed to achieve miscellaneous applications, including optical parametric oscillation, frequency comb generation, electro-optic modulation, and single-photon sources, making possible monolithic SiC quantum integrated circuits [3–8]. Among more than 200 crystalline SiC polytypes, 4H-SiC is one of the most widely used polytypes for integrated photonics, due to its high crystal quality and low optical loss [5]. As a uniaxial crystal, 4H-SiC exhibits orientation-dependent and polarization-dependent optical properties, including linear refractive index and nonlinear refractive index. It means that the transverse-electric (TE) and transverse-magnetic (TM) polarized light, propagating along the 4H-SiC waveguides, typically has different properties, such as polarization-dependent loss, polarization-dependent dispersion, and polarization-dependent nonlinear strength [9]. Thus, polarization control and management in the 4H-SiC integrated platform are highly important, and are worthy exploring.

The polarization beam splitter (PBS), a key component for polarization manipulation, enables two orthogonal mode separation and provides polarization diversity in photonic integrated circuits, which can also be applied for polarization division multiplexing and polarization entanglement quantum systems [10,11]. Many different types of PBSs have been studied in silicon-on-insulator integrated platforms (for example, directional couplers, multimode interferometers, gratings, and plasmonic waveguides) [12–17]. Although silicon ($n = 3.5$ at 1550 nm) does not have material-based birefringence, high geometric birefringence in silicon waveguides makes easy polarization beam splitting, as the phase-matching condition cannot be satisfied by two orthogonal modes simultaneously due to the large effective refractive index contrast. Waveguides, made of optical materials with lower refractive index, such as SiC ($n = 2.6$), silicon nitride (SiN) ($n = 2.0$), and lithium niobate ($LiNbO_3$) ($n = 2.2$) at 1550 nm, usually require larger geometry to confine the light and have lower birefringence compared to silicon waveguides. For example, the effective refractive index of the fundamental TE and TM modes in a typical standard single-mode silicon waveguide with a dimension of 220 nm × 500 nm at 1550 nm [13,14], is 2.39 and 1.59,

respectively, but becomes 1.79 and 1.63, respectively, in a typical single-mode 4H-SiC waveguide with a dimension of 350 nm × 560 nm [1], which shows much lower birefringence. Therefore, it is a challenge to make compact and efficient PBSs in the relatively low-refractive-index optical materials-based integrated platforms [18].

Several methods have been proposed and demonstrated in $LiNbO_3$ and SiN integrated platforms. Multimode interferometers and Mach–Zehnder interferometers are the most promising approaches to make good-performance PBSs with low-refractive-index optical materials [18–21]. Especially, a high extinction ratio (>20 dB) can be achieved by tailoring the phase-shifting region. However, such devices usually have a large footprint of thousands of square micrometers, which is not good for compactness and high-density integration. Metamaterial has been proposed to design an anisotropic medium with artificially generated strong birefringence, making possible efficient PBSs, but complex structures with high-precision fabrication are needed [22]. Three-dimensional multiple-layer structures and assisted amorphous silicon waveguides offer the capability to make efficient and broadband PBSs, but introducing extra layers or materials requires multiple lithography and complicated fabrication processing [23,24]. Cascaded asymmetric directional couplers, which convert fundamental TM modes to first-order modes, enable high-performance PBSs, fabricated by a standard single-step lithography process, and the device length is as short as 112 μm [25]. Generally, it remains a demanding challenge to achieve ultra-compact and efficient low-birefringence PBSs, conforming to simple fabrication processes, and there is also a lack of PBSs in SiC integrated platforms.

In this work, we design a novel vertical-dual-slot waveguide (VDSW) based PBS for low-birefringence waveguides. Vertical-dual-slot waveguides have been used for group velocity dispersion tailoring and efficient electro-optic modulation by enhancing the optical and electric field overlap [26,27]. Here, we use this structure to adjust the mode distribution for polarization splitting. It is found that the TM mode is particularly sensitive to the VDSW with regard to mode distribution. By adjusting the TM mode distribution, the coupling strength between the two waveguides is strongly modulated. The simple structure is also compatible with the standard single-step lithography fabrication process. We also experimentally demonstrate the PBS in the 4H-SiC-on-insulator (SiCOI) integrated platform. The device exhibits low insertion loss of <0.71 dB and <0.51 dB for the TE and TM polarized light, respectively, and polarization extinction ratio of >13 dB from 1540 nm to 1620 nm, within a very small coupling region of 2.2 μm × 15 μm. To our best knowledge, this is the first demonstration of a PBS in a SiC integrated platform.

2. DESIGN AND SIMULATION

Figure 1 shows the schematic of the proposed VDSW-based PBS, and the inset shows the cross section of the coupling region of the PBS, which consists of two cores, four air slots, and three strips. The central core is a single-mode 4H-SiC waveguide and has a dimension of 400 nm × 600 nm. The slot has a width of Δd, and the side strip has a width of w_s, with

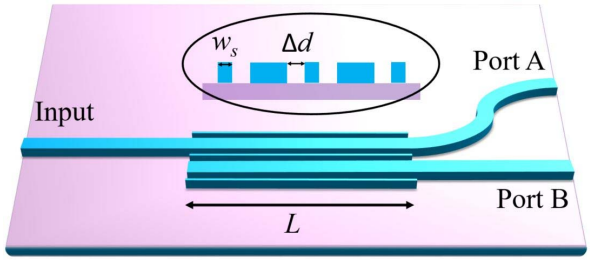

Fig. 1. Schematic of the proposed PBS with VDSWs.

the same height as the central core. The coupling region, with a length of L, is composed of two parallel VDSWs, sharing the same side strip in between. Light is injected into the single-mode waveguide (SMW) from the left input port. After the PBS, the TE-polarized light remains in the upper waveguide and goes out from Port A, while the TM-polarized light couples into the other waveguide and goes out from Port B.

We design and simulate the PBS using Lumerical MODE and FDTD software packages. The energy density distribution of the TE and TM modes in the 4H-SiC SMWs and the VDSWs is shown in Fig. 2. It is seen that both TE and TM modes are well confined in the SMWs and have a similar effective refractive index of 1.90 and 1.78, respectively. The effective mode area of the TE and TM modes is 0.38 μm^2 and 0.47 μm^2, respectively. However, when employing the vertical-dual-slot structure, for example, with a dimension of $w_s = 200$ nm and $\Delta d = 100$ nm, the TM mode distribution can be largely changed, but the TE mode distribution remains almost unchanged. The effective refractive index of the TE and TM modes is 1.92 and 1.82, respectively, almost the same as those in the SMW, but the effective mode area of TE and TM modes becomes 0.37 μm^2 and 0.57 μm^2, respectively. The TM mode distribution is much more strongly affected by the vertical-dual-slot structure, especially with an apparent lateral expansion, compared to the TE mode. The strong polarization-dependent mode distribution modulation provides

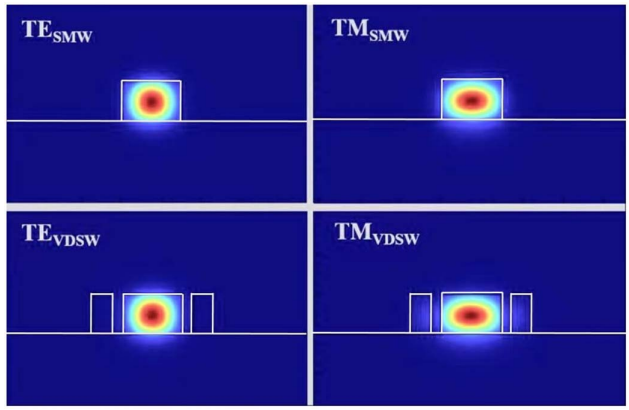

Fig. 2. Energy density profiles of TE and TM modes in the 4H-SiC SMWs and the VDSWs. In the simulation, the SMW has a dimension of 400 nm × 600 nm, the VDSW has a strip width of 200 nm and a slot width of 100 nm, the refractive index of the SiC is 2.56 and 2.60 for the TE and TM mode, respectively, and the refractive index of the SiO_2 is 1.44.

the opportunity to realize compact and efficient polarization beam splitting with the proposed structure.

We optimize three parameters in the VDSW-based PBS, including the side strip width, the slot width, and the coupling length. The minimal side strip width and the slot width are limited by the minimal feature size of the fabrication process, which is about 100 nm. The coupling length of the TM mode is estimated to be 17.3 μm, according to the coupling theory of the directional couplers, given by $L = \frac{\lambda}{2(n_{even}-n_{odd})}$, where λ is the wavelength of the light, and $n_{even} = 1.837$ and $n_{odd} = 1.792$ are its effective refractive index of the even symmetric mode and the odd symmetric mode, respectively [28]. The coupling length of the TE mode is 97 μm, much longer than that of the TM mode. The transmission efficiency versus the coupling length is plotted in Fig. 3(a), with fixed side strip width and slot width of 200 and 100 nm, respectively. The transmission of TE-polarized light decreases with the coupling length. The highest transmission of TM-polarized light is between 17 and 18 μm, matching the calculation well. However, the performance of the TE-polarized light is not as good as that of the TM-polarized light propagating through the PBS within this range, but has lower coupling efficiency and higher cross talk. Thus, we choose the crossing point from Fig. 3(a), which is at 15 μm, so that both TE- and TM-polarized light can have high transmission efficiency and large polarization extinction ratio, given by $ER_{TE} = 10\log_{10}\frac{T_{TE_{Port\ A}}}{T_{TE_{Port\ B}}}$ and $ER_{TM} = 10\log_{10}\frac{T_{TM_{Port\ B}}}{T_{TM_{Port\ A}}}$, for TE- and TM-polarized light, respectively. Within the coupling length range from 14.5 to 15.5 μm, both TE- and TM-polarized light has a high transmission efficiency of >90%, equivalent to an insertion loss of <0.46 dB, given by $IL_{TE} = -10\log_{10}T_{TE_{Port\ A}}$ and $IL_{TM} = -10\log_{10}T_{TM_{Port\ B}}$, for TE- and TM-polarized light, respectively, and a polarization extinction ratio of >12 dB. The transmission efficiency versus the side strip width is plotted in Fig. 3(b), with fixed slot width and coupling length of 100 nm and 15 μm, respectively. The transmission efficiency of the TE-polarized light increases with the side strip width, while that of the TM-polarized light decreases. The narrow side strip width enables efficient TM-polarized light coupling, but results in high cross talk of the TE-polarized light, due to the close distance between the two coupling central waveguides. Wide side strip width could suppress the TE-polarized light coupling, but also weaken the TM-polarized light coupling, in spite of strong TM mode distribution modulation. Within the side strip width range from 160 to 220 nm, both TE- and TM-polarized light beams have a high transmission efficiency of >90% and a polarization extinction ratio of >12 dB. Such a wide side strip width range allows a high fabrication dimension tolerance. The transmission efficiency versus the slot width is plotted in Fig. 3(c), with fixed side strip width and coupling length of 200 nm and 15 μm, respectively. It can be seen that the device is more sensitive to the slot width than to the side strip width. The transmission efficiency of the TE-polarized light increases with the increasing slot width, while that of the TM-polarized light first increases and then decreases. The narrow slot width expands the TM mode intensively and compresses the TE mode at the same time, but with the current coupling length, the TM-polarized light does not have enough power coupling, and the close distance between the two coupling central waveguides results in high cross talk. The wide slot width helps to increase the transmission efficiency of the TE-polarized light, but also reduces the TM-polarized light coupling due to the weak TM mode distribution modulation and the long distance between the two coupling central waveguides. Within the slot distance range from 90 to 105 nm, both TE- and TM-polarized light beams have a high transmission efficiency of >90% and a polarization extinction ratio of >12 dB.

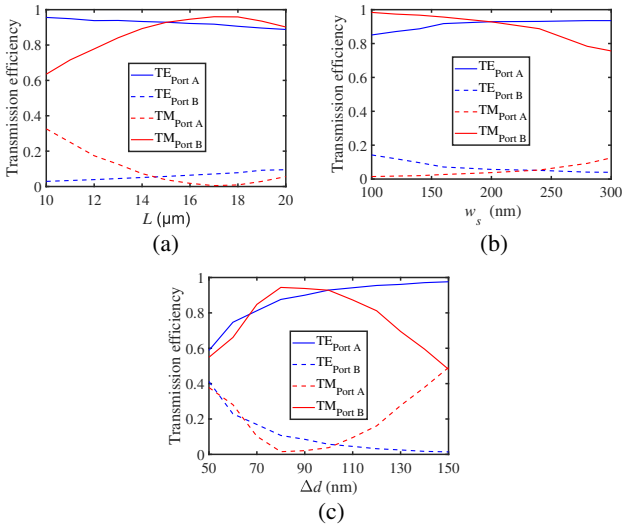

Fig. 3. Simulated results of the transmission efficiency as a function of (a) the coupling length with a side strip width of 200 nm and a slot width of 100 nm, (b) the side strip width with a slot width of 100 nm and a coupling length of 15 μm, and (c) the slot width with a side strip width of 200 nm and a coupling length of 15 μm.

Taking comprehensive consideration of high transmission efficiency, high polarization extinction ratio, low cross talk, and fabrication feasibility, we select the side strip width, the slot width, and the coupling length of 200 nm, 100 nm, and 15 μm, respectively, as the optimized parameters of the VDSW-based PBS in the 400 nm thick 4H-SiC integrated platform. The simulated TE- and TM-polarized light propagation at 1550 nm in the optimized PBS is shown in Fig. 4. As can be seen, the TE-polarized light is directly guided in the upper waveguide, while the TM-polarized light is coupled into the adjacent waveguide, indicating that the proposed structure works effectively. The transmission efficiency and the polarization extinction ratio versus the wavelength are then simulated

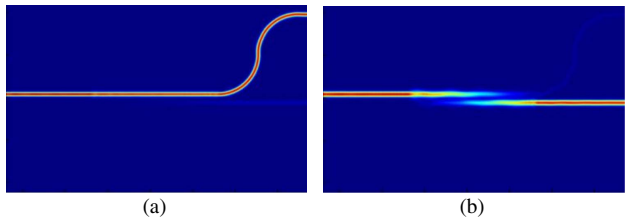

Fig. 4. (a) TE- and (b) TM-polarized light propagation along the optimized PBS.

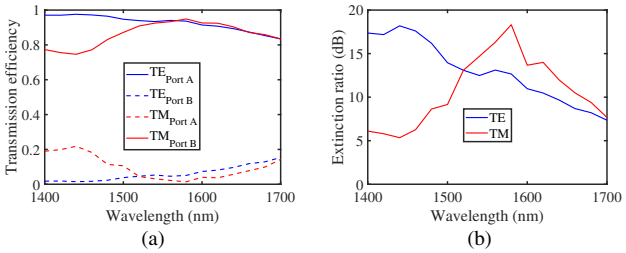

Fig. 5. Simulated results of (a) transmission efficiency and (b) polarization extinction ratio as a function of wavelength.

and plotted in Fig. 5. Within the wavelength range between 1510 and 1580 nm, both TE- and TM-polarized light beams have a high transmission efficiency of >90%, equivalent to an insertion loss of <0.46 dB, with a corresponding polarization extinction ratio >12.5 dB.

3. FABRICATION

After optimizing the PBS parameters, we fabricate the device on the 4H-SiCOI chip. We fabricate the 4H-SiCOI chip through the ion-cut method, shown in Fig. 6(a).

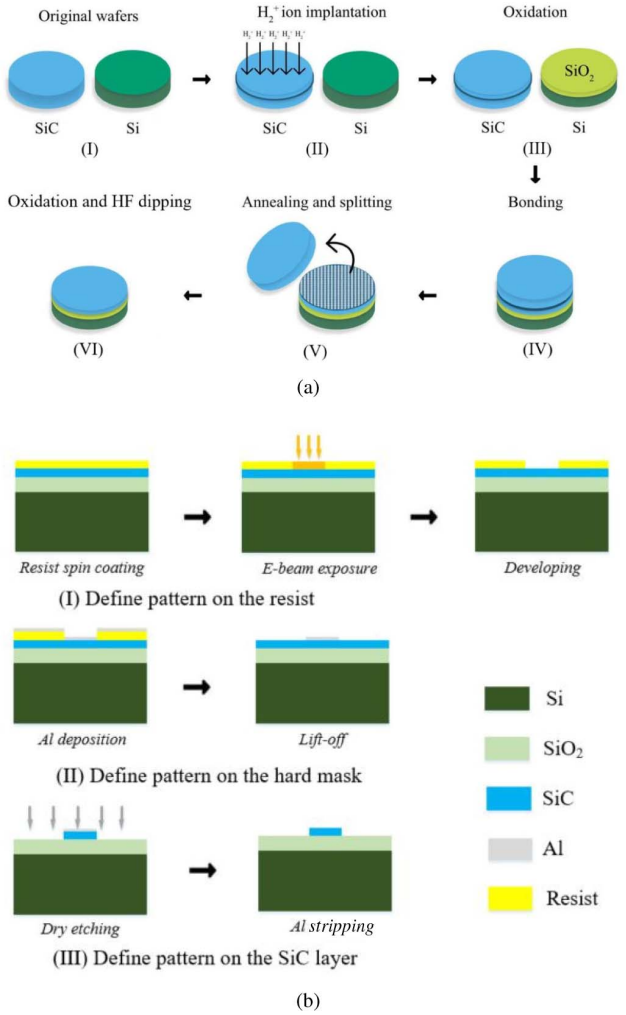

Fig. 6. (a) Process flow of the 4H-SiCOI stack fabrication; (b) process flow of the 4H-SiC photonic device fabrication.

First, a high-purity semi-insulating 4H-SiC wafer is implanted with dihydrogen cations, which is on-axis cut with the extraordinary optical axis parallel to the *c* axis of the crystal and perpendicular to the wafer plane, with energy of 340 keV and dose of 6×10^{16} cm^{-2} at 200°C to generate a damaged layer underneath the wafer surface at a depth of 1.26 μm. Second, a silicon wafer, as the substrate, is thermally oxidized to form 2.42 μm thick SiO_2 as a buried oxide layer. Third, the two wafers are cleaned through a reverse Radio Corporation of America (RCA) cleaning process, and are bonded via hydrophilic bonding. Fourth, the bonded wafers are annealed at 800°C for 6 h to split the 4H-SiC wafer, and a thin 4H-SiC film remains on the Si – SiO_2 substrate to form the 4H-SiCOI stack. Fifth, the thickness of the 4H-SiC thin film is reduced down to ∼400 nm via thermal oxidation and HF dipping. Within a 1 cm^2 4H-SiCOI chip, the thickness of the 4H-SiC thin film is 404 ± 1 nm, and the surface roughness is 1.2 ± 0.3 nm, indicating a good uniformity and smoothness. A scanning electron microscope (SEM) image of the cross section of the 4H-SiCOI stack is shown in Fig. 7(a). An atomic force microscopy (AFM) image of the chip surface profile is shown in Fig. 7(b).

After the 4H-SiCOI chip preparation, we fabricate the device on the chip, shown in Fig. 6(b). First, the pattern is defined on the positive electron-beam (e-beam) resist, AR-P 6200.09, through the e-beam writer (JEOL JBX-9500FSZ). Second, the pattern is transferred to an aluminum metal mask through the e-beam evaporation and a lift-off process. Finally, the pattern is transferred to the 4H-SiC thin film by inductively coupled plasmon reactive ion etching. The SEM image of the fabricated device is shown in Fig. 8(a). At every input and the output port

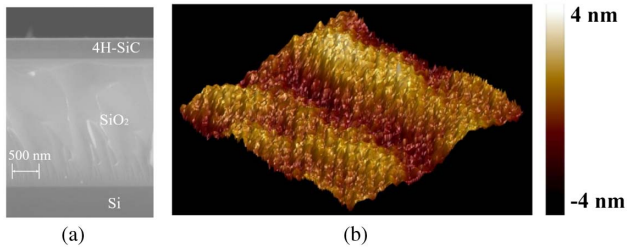

Fig. 7. (a) SEM image of the 4H-SiCOI stack; (b) AFM image of the 4H-SiCOI surface topography within an area of 1 μm × 1 μm.

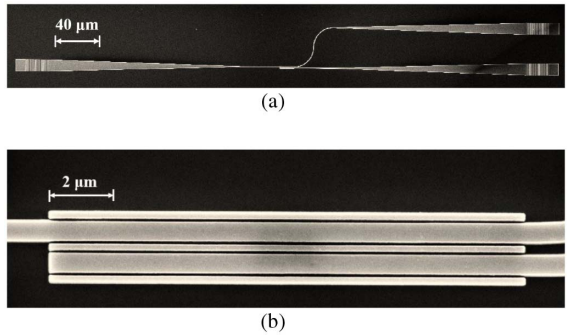

Fig. 8. (a) SEM image of the fabricated testing device; (b) zoom-in SEM image of the fabricated VDSW-based PBS.

of the beam splitters, polarization-insensitive grating couplers are connected for the device performance characterization [9]. A zoom-in SEM image of the VDSW-based PBS is shown in Fig. 8(b).

4. CHARACTERIZATION

We build the measurement setup, shown in Fig. 9, to test the device. A tunable continuous-wave laser source (ANDO AQ4321D) launches light into a polarization controller to adjust the polarization to quasi-TE or quasi-TM mode. The polarized light is coupled in and out of the device with a pair of cleaved fibers mounted on the fiber holders. The output light is detected by an optical spectrum analyzer (ANDO AQ6317B), which allows synchronized sweep with the tunable laser source to measure the transmission spectrum.

The normalized transmission efficiency in the VDSW-based PBS of the TE- and TM-polarized light coupling out of Port A and Port B is plotted in Fig. 10(a). The normalized transmission has already excluded the grating transmission for each polarization, and only shows the PBS performance. As can be seen, the transmittance of the TE- and TM-polarized light in Port A and Port B, respectively, is very high and flat, within the measured wavelength range between 1520 and 1620 nm. The transmission efficiency of TE- and TM-polarized light is >85% and >89%, equivalent to an insertion loss of <0.71 dB and <0.51 dB, respectively. The trend of the transmission efficiency for both TE- and TM-polarized light versus the wavelength almost matches the simulation, but the spectrum has a slight redshift, as there is supposed to be a peak at around 1580 nm, according to Fig. 5(a). This could be due to the linewidth variation and fabrication imperfections in the fabrication processes. Meanwhile, the device also exhibits a low cross talk because the transmission efficiency of the TE-polarized light in Port B and the TM-polarized light in Port A is very low. The polarization extinction ratio versus the wavelength is plotted in Fig. 10(b). As can been seen, the polarization extinction ratio is >10 dB within the measured wavelength range for both TE- and TM-polarized light. Especially, the polarization extinction ratio is >13 dB, between 1540 and 1620 nm. Compared to the simulation results, the measured polarization extinction ratio of TE-polarized light is a little higher, while that of the TM-polarized light is a little lower, which is considered to be due to the polarization-dependent propagation loss and coupling loss in the VDSW coupling region, due to the mode distribution and sidewall roughness.

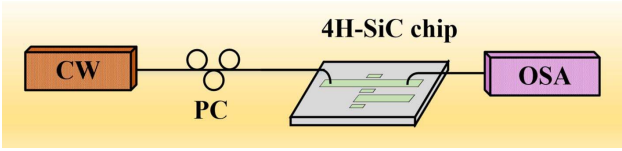

Fig. 9. Measurement setup schematic. CW, tunable continuous-wave laser; PC, polarization controller; OSA, optical spectrum analyzer.

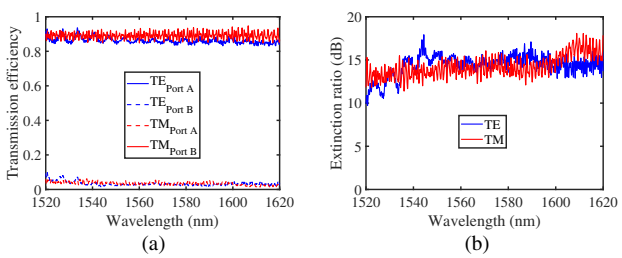

Fig. 10. Measured results of (a) normalized transmission efficiency and (b) polarization extinction ratio versus wavelength.

5. CONCLUSION

In this paper, a novel VDSW-based coupling scheme is proposed for low-birefringence polarization beam splitting and is experimentally demonstrated in the 4H-SiCOI integrated platform. The PBS is very small, with a footprint of 2.2 μm × 15 μm, which benefits compactness and high-density integration. The measurement results show that it has very low insertion loss of <0.71 dB and <0.51 dB for the TE- and TM-polarized light, respectively, within 100 nm operational bandwidth, and a polarization extinction ratio of >13 dB for both TE- and TM-polarized light, within 80 nm operational bandwidth, covering most of the C-band and the whole L-band. Our work provides a new solution to splitting the light beam with low birefringence, and paves the way for the polarization diversity applications in the relatively low-refractive-index material-based integrated platforms with high compactness.

Funding. Horizon 2020 Framework Programme (824096); H2020 Future and Emerging Technologies (899679).

Disclosures. The authors declare no conflicts of interest.

Data Availability. Data underlying the results presented in this paper are not publicly available at this time but may be obtained from the authors upon reasonable request.

REFERENCES

1. D. M. Lukin, C. Dory, M. A. Guidry, K. Y. Yang, S. D. Mishra, R. Trivedi, M. Radulaski, S. Sun, D. Vercruysse, G. H. Ahn, and J. Vučković, "4H-silicon-carbide-on-insulator for integrated quantum and nonlinear photonics," Nat. Photonics **14**, 330–334 (2020).
2. S. Castelletto and A. Boretti, "Silicon carbide color centers for quantum applications," J. Phys. Photon. **2**, 022001 (2020).
3. X. Shi, W. Fan, A. K. Hansen, M. Chi, A. Yi, X. Ou, K. Rottwitt, and H. Ou, "Thermal behaviors and optical parametric oscillation in 4H-silicon carbide integrated platforms," Adv. Photon. Res. **2**, 2100068 (2021).
4. C. Wang, Z. Fang, A. Yi, B. Yang, Z. Wang, L. Zhou, C. Shen, Y. Zhu, Y. Zhou, R. Bao, Z. Li, Y. Chen, K. Huang, J. Zhang, Y. Cheng, and X. Ou, "High-Q microresonators on 4H-silicon-carbide-on-insulator platform for nonlinear photonics," Light Sci. Appl. **10**, 139 (2021).
5. M. A. Guidry, K. Y. Yang, D. M. Lukin, A. Markosyan, J. Yang, M. M. Fejer, and J. Vučković, "Optical parametric oscillation in silicon carbide nanophotonics," Optica **7**, 1139–1142 (2020).
6. M. A. Guidry, D. M. Lukin, K. Y. Yang, R. Trivedi, and J. Vučković, "Quantum optics of soliton microcombs," arXiv:2103.10517 (2021).
7. T. Fan, X. Wu, S. R. Vangapandu, A. H. Hosseinnia, A. A. Eftekhar, and A. Adibi, "Racetrack microresonator based electro-optic phase shifters on a 3C silicon-carbide-on-insulator platform," Opt. Lett. **46**, 2135–2138 (2021).

8. S. Castelletto, B. C. Johnson, and A. Boretti, "Quantum effects in silicon carbide hold promise for novel integrated devices and sensors," Adv. Opt. Mater. **1**, 609–625 (2013).
9. X. Shi, W. Fan, Y. Lu, A. K. Hansen, M. Chi, A. Yi, X. Ou, K. Rottwitt, and H. Ou, "Polarization and spatial mode dependent four-wave mixing in a 4H-silicon carbide microring resonator," APL Photon. **6**, 076106 (2021).
10. Y. Tan, H. Wu, and D. Dai, "Silicon-based hybrid (de)multiplexer for wavelength-/polarization-division-multiplexing," J. Lightwave Technol. **36**, 2051–2058 (2018).
11. E. Meyer-Scott, N. Prasannan, C. Eigner, V. Quiring, J. M. Donohue, S. Barkhofen, and C. Silberhorn, "High-performance source of spectrally pure, polarization entangled photon pairs based on hybrid integrated-bulk optics," Opt. Express **26**, 32475–32490 (2018).
12. J. Wang, D. Liang, Y. Tang, D. Dai, and J. E. Bowers, "Realization of an ultra-short silicon polarization beam splitter with an asymmetrical bent directional coupler," Opt. Lett. **38**, 4–6 (2013).
13. H. Zafar, M. F. Pereira, K. L. Kennedy, and D. H. Anjum, "Fabrication-tolerant and CMOS-compatible polarization splitter and rotator based on a compact bent-tapered directional coupler," AIP Adv. **10**, 125214 (2020).
14. C. Errando-Herranz, S. Das, and K. B. Gylfason, "Suspended polarization beam splitter on silicon-on-insulator," Opt. Express **26**, 2675–2681 (2018).
15. D. Dai, Z. Wang, J. Peters, and J. E. Bowers, "Compact polarization beam splitter using an asymmetrical Mach–Zehnder interferometer based on silicon-on-insulator waveguides," IEEE Photon. Technol. Lett. **24**, 673–675 (2012).
16. C. Li, M. Zhang, J. E. Bowers, and D. Dai, "Ultra-broadband polarization beam splitter with silicon subwavelength-grating waveguides," Opt. Lett. **45**, 2259–2262 (2020).
17. J. Chee, S. Zhu, and G. Lo, "CMOS compatible polarization splitter using hybrid plasmonic waveguide," Opt. Express **20**, 25345–25355 (2012).
18. S. Gao, Y. Wang, K. Wang, and E. Skafidas, "Low-loss and broadband 2 ×2 polarization beam splitter based on silicon nitride platform," IEEE Photon. Technol. Lett. **28**, 1936–1939 (2016).
19. R. Kudalippalliyalil, T. E. Murphy, and K. E. Grutter, "Low-loss and ultra-broadband silicon nitride angled MMI polarization splitter/combiner," Opt. Express **28**, 34111–34122 (2020).
20. H. Xu, D. Dai, L. Liu, and Y. Shi, "Proposal for an ultra-broadband polarization beam splitter using an anisotropy-engineered Mach-Zehnder interferometer on the *x*-cut lithium-niobate-on-insulator," Opt. Express **28**, 10899–10908 (2020).
21. J. Zhan, J. Brock, S. Veilleux, and M. Dagenais, "Silicon nitride polarization beam splitter based on polarization-independent MMIS and apodized Bragg gratings," Opt. Express **29**, 14476–14485 (2021).
22. C. Deng, M. Lu, Y. Sun, L. Huang, D. Wang, G. Hu, R. Zhang, B. Yun, and Y. Cui, "Broadband and compact polarization beam splitter in LNOI hetero-anisotropic metamaterials," Opt. Express **29**, 11627–11634 (2021).
23. L. Zhang, X. Fu, and L. Yang, "Compact, broadband and low-loss polarization beam splitter on lithium-niobate-on-insulator using a silicon nanowire assisted waveguide," IEEE Photon. J. **12**, 6601906 (2020).
24. J. Feng and R. Akimoto, "A three-dimensional silicon nitride polarizing beam splitter," IEEE Photon. Technol. Lett. **26**, 706–709 (2014).
25. B. Bhandari, C.-S. Im, O. R. Sapkota, and S.-S. Lee, "Highly efficient broadband silicon nitride polarization beam splitter incorporating serially cascaded asymmetric directional couplers," Opt. Lett. **45**, 5974–5977 (2020).
26. S. Shi and D. W. Prather, "Ultrabroadband electro-optic modulator based on hybrid silicon-polymer dual vertical slot waveguide," Adv. Optoelectron. **2011**, 714895 (2011).
27. K. Guo, L. Lin, J. B. Christensen, E. N. Christensen, X. Shi, Y. Ding, K. Rottwitt, and H. Ou, "Broadband wavelength conversion in a silicon vertical-dual-slot waveguide," Opt. Express **25**, 32964–32971 (2017).
28. B. E. Little and W.-P. Huang, "Coupled-mode theory for optical waveguides," Prog. Electromagn. Res. **10**, 217–270 (1995).